Dynamics Study on the Anti-Human Immunodeficiency Virus Chemokine Viral Macrophage-Inflammatory Protein-II (VMIP-II) Reveals a Fully Monomeric Protein†

Andy C. LiWang,‡ Jian Jing Cao,§ Hong Zheng,|| Zhaohai Lu,|| Stephen C. Peiper,|| and Patricia J. LiWang*,§

Departments of Chemistry and of Medicinal Chemistry and Medical Pharmacology, Purdue University, West Lafayette, Indiana 47907-1393, and James Graham Brown Cancer Center, University of Louisville, Louisville, Kentucky 40202

Received May 28, 1998; Revised Manuscript Received September 14, 1998

ABSTRACT: Encoded by Kaposi's sarcoma-associated herpesvirus, viral macrophage-inflammatory protein-II (VMIP-II) is unique among CC chemokines in that it has been shown to bind to the CXC chemokine receptor CXCR4 as well as to a variety of CC chemokine receptors. This unique binding ability allows vMIP-II to block infection by a wide range of human immunodeficiency virus type I (HIV-1) strains, but the structural and dynamic basis for this broad range of binding is not known. ^{15}N T_1, T_2 and $^{15}N\{-H^N\}$ nuclear Overhauser effect (NOE) values of vMIP-II, determined through a series of heteronuclear multidimensional nuclear magnetic resonance (NMR) experiments, were used to obtain information about the backbone dynamics of the protein. Whereas almost all chemokine structures reveal a dimer or multimer, vMIP-II has a rotational correlation time (τ_c) of 4.7 ± 0.3 ns, which is consistent with a monomeric chemokine. The rotational diffusion anisotropy, $D_{\|}/D_{\perp}$, is approximately 1.5 ± 0.1. The conformation of vMIP-II is quite similar to other known chemokines, containing an unstructured N-terminus followed by an ordered turn, three β-strands arranged in an antiparallel fashion, and one C-terminal α-helix that lies across the β-strands. Most of the protein is well-ordered on a picosecond time scale, with an average order parameter S^2 (excluding the N-terminal 13 amino acids) of 0.83 ± 0.09, and with even greater order in regions of secondary structure. The NMR data reveal that the N-terminus, which in other chemokines has been implicated in receptor binding, extends like a flexible tail in solution and possesses no secondary structure. The region of the ordered turn, including residues 25−28, experiences conformational exchange dynamics. The implications of these NMR data to the broad receptor binding capability of vMIP-II are discussed.

Chemotactic cytokines (chemokines) are a family of proteins active in the immune system that mediate inflammation, chemotaxis, and host defense (*1*, *2*). In addition to these functions, some chemokines have been shown to inhibit infection by HIV-1 (*3*). This activity derives from the requirement of HIV-1 for a chemokine receptor as a cofactor for entry into the cell; the binding of some chemokines to their natural receptor blocks this binding by HIV-1 and prevents infection (*4*−*8*). The chemokines have been subdivided into two major subfamilies, based on the placement of canonically conserved cysteine residues near the N-terminus: The CC subfamily has contiguous cysteines and includes such proteins as MIP-1β, MIP-1α, and RANTES. The CXC subfamily, so named because a single amino acid separates the conserved cysteines, includes IL-8, PF-4, and MGSA. Several chemokine receptors have been identified, and while a particular receptor often will bind several members of one subfamily, no cross-binding has been observed between a receptor for one subfamily and a wild-type mammalian chemokine of the other subfamily, with the exception of the Duffy receptor in red blood cells, which binds to selected CC and CXC chemokines (ref *9* and references therein; *10*).

The lack of receptor cross-binding may have its origins in the different structures observed for the two subfamilies of chemokines. Most reported chemokine structures reveal a multimeric protein, typically a dimer (*11*−*20*). However, despite the fact that the chemokine monomer fold is similar for both subfamilies, members of the CC subfamily form a dimer that is structurally distinct from that of members of the CXC subfamily: with one possible exception (*15*) the CC chemokine dimer interface is found at the N-terminus

† Funding was provided by an American Cancer Society Institutional Grant through the Purdue Cancer Center.

* To whom correspondence should be addressed: Phone (765) 494-8519; Fax (765) 494-0239; e-mail liwang@chem.purdue.edu.

‡ Department of Medicinal Chemistry and Medical Pharmacology, Purdue University.

§ Department of Chemistry, Purdue University.

|| University of Louisville.

[1] Abbreviations: CC chemokines include MIP-1β, macrophage inflammatory protein 1β; MIP-1α, macrophage inflammatory protein 1α; MCP, monocyte chemoattractant protein; and RANTES, regulated on activation of normal T cell expressed and secreted. CXC chemokines include IL-8, interleukin 8; MGSA, melanoma growth-stimulatory activity; NAP-2, neutrophil-activating peptide 2; and PF-4, platelet factor 4. HIV-1, human immunodeficiency virus type 1; NMR, nuclear magnetic resonance; HSQC, heteronuclear single quantum coherence; HMQC, heteronuclear multiple quantum coherence; rf, radio frequency; DSS, 2,2-dimethyl-2-silapentane-5-sulfonate, sodium salt; EDTA, ethylenediaminetetraacetic acid.

10.1021/bi9812726 CCC: $18.00
Published on Web 12/04/1998

(*11*, *13*, *16*, *17*, *19*), while the CXC chemokine dimer interface is formed by completely different residues, along the β1 strand near the middle of the protein sequence (*12*, *14*, *20*). In recent years the physiologic relevance of the chemokine dimer has been questioned, as it has been shown that some CXC chemokines are active after modification that produces demonstrably monomeric protein (*21*−*24*). However, the presence of a multimeric chemokine at the cellular surface has been indicated by recent studies that have shown that cell surface sugars act to locally concentrate chemokines (*25*), and that indeed chemokines are most active in blocking HIV in the presence of heparan or proteoglycans (*26*). In addition, some studies directly point to an active multimeric chemokine (*27*, *28*).

Until recently, data suggested that the distinct activities of CC and CXC chemokines to engage their cognate receptors extended to their anti-HIV properties, with certain CC chemokines (MIP-1β, MIP-1α, and RANTES) being uniquely able to block HIV strains that use the CCR5 and CCR3 receptors for entry (*4*−*6*), while only the CXC chemokine SDF-1 could block infection by HIV strains that utilize the CXC receptor CXCR4 (*7*, *8*). But it was recently reported that a chemokine encoded by Kaposi's sarcoma-associated herpesvirus (*29*) was the first known wild-type protein that could bind to both CC and the CXC chemokine receptors and therefore could block infection by diverse HIV strains (*30*, *31*). Therefore, this chemokine (called vMIP-II) is both medically important and biochemically distinct from other chemokines. vMIP-II is a CC chemokine that shares greatest sequence identity to human MIP-1α and MIP-1β at about 40% for each (*29*). However, despite this overall high level of identity, the N-terminal amino acids of vMIP-II are not identical in many positions relative to MIP-1β and MIP-1α, nor is the N-terminal region of vMIP-II strikingly similar to that of the CXC chemokine SDF-1 (*31*). As the N-termini of chemokines of both subfamilies have been implicated in function (*32*−*36*), this distinct N-terminus likely plays a role in the unique activity of vMIP-II. As vMIP-II possesses the most broad anti-HIV capability among chemokines, it has emerged as a model for potential anti-HIV therapeutics, and the structural and dynamic basis for its potent activity is of great interest.

We report the backbone dynamics of the chemokine vMIP-II, which is the first such report for a CC chemokine and is only the second report of this type for a protein in the chemokine family (*37*). To allow interpretation of the dynamics data, we also have determined the secondary structure and fold of the protein, showing that vMIP-II has the standard chemokine fold that is found for all other proteins in the family (*11*−*20*). However, vMIP-II is unusual in that it is demonstrably monomeric even under the high concentrations (~1 mM) required for NMR measurements. In addition, while most of the protein is quite ordered on the picosecond time scale (particularly within regions of secondary structure), the N-terminus, which is where the putative receptor binding site resides, is highly disordered. In addition, the ordered turn preceding strand β1 undergoes conformational exchange, even after accounting for global rotational diffusion anisotropy.

MATERIALS AND METHODS

Production and Purification of vMIP-II. The gene for vMIP-II was kindly provided by Dr. Patrick Moore and Dr. Yuan Chang, Columbia University. vMIP-II was expressed in the Novagen (Milwaukee, WI) pET32a(+) expression vector, which allows production of the desired protein along with a thioredoxin fusion tag. The vector containing the sequence encoding the mature form of vMIP-II was transformed into BL21(DE3) and an individual colony was subsequently grown in 1 L of minimal medium containing $^{15}NH_4Cl$ (Martek Biosciences, Columbia, MD) as the only nitrogen source, and with either $^{13}C_6$-glucose (Isotec, Miamisburg, OH) or unlabeled glucose. Cells were induced at $A_{550} = 0.9$ by making the cell culture 1 mM in IPTG (Calbiochem, La Jolla, CA) and harvested by centrifugation after 3.5 h (for the ^{15}N, ^{13}C preparation) or 12 h (for the ^{15}N preparations). The cell pellet was resuspended in 500 mM NaCl, 20 mM Tris, pH 8, and 10 mM benzamidine and then passed through a French press two times at 16 000 psi, then centrifuged at 19000*g* for 1 h. The resulting pellet was then resuspended in 15 mL of 5 M guanidine hydrochloride, 500 mM NaCl, 20 mM Tris, pH 8, 5 mM imidazole, and 5 mM β-mercaptoethanol (overall buffer adjusted to pH 8). The resuspended protein was centrifuged at 15000*g* for 30 min to remove insoluble material. The protein solution was loaded onto a Ni chelating column (Pharmacia, Piscataway, NJ), eluted with imidazole, and subjected to refolding (*38*). The resulting purified thioredoxin−vMIP-II fusion protein was then dialyzed against 50 mM Tris, pH 8. Cleavage of the thioredoxin fusion tag was carried out in 50 mM Tris, pH 8, and 2 mM $CaCl_2$ with recombinant enterokinase (Novagen). This results in an N-terminal Ala-Met-Ala on the protein. The cleaved protein was purified by C4 reversed-phase chromatography, using a Vydac column (Hesperia, CA) and the Bio-Logic system (Bio-Rad Hercules, CA). Protein samples were lyophilized and for NMR samples the protein was dissolved in 10 mM sodium phosphate, pH 2.5, for all chemical shift assignments and structural work. For the high-pH control, one-third of the sample at pH 2.5 was lyophilized and dissolved in 10 mM sodium phosphate, pH 5.3 (measured pH of the sample was 5.1). All NMR samples were made to 5% D_2O (Isotec).

NMR Spectroscopy. All spectra were recorded at 25 °C on a Varian UnityPlus 600 MHz spectrometer, equipped with a z-shielded gradient triple resonance probe. Sample tubes were from Shigemi Inc. (Allison Park, PA). Chemical shift referencing is relative to DSS, using the method proposed by Wishart et al. (*39*).

The ^{15}N HSQC was recorded as a 160* × 512* 2D matrix in the t_1 and t_2 dimensions, respectively, where n* represents n complex points. H_2O flip-back pulses were implemented to minimize saturation of water (*40*). Acquisition times in each dimension were 105.0 (t_1) and 64.0 ms (t_2), and the total duration of the experiment was 1.53 h. The data were apodized along t_2 by using a 90°-shifted squared sine-bell, truncated at 1% ($\sin^2 175°$). The t_1 time domain was extended to 240* by using mirror-image linear prediction (8 coefficients) (*41*) and then apodized with an untruncated 90°-shifted squared sine-bell. Prior to Fourier transform, the data were zero-filled to a digital resolution of 3.0 (F_1) and 5.2 Hz (F_2).

The CBCA(CO)NH spectrum (*42*) was recorded as a 34* × 60* × 512* 3D matrix with acquisition times of 22.3 (t_1, ^{15}N), 7.1 (t_2, $^{13}C^{\alpha,\beta}$), and 63.5 ms (t_3, $^1H^N$). The total acquisition time was 38.4 h. Acquired data were apodized with a 90°-shifted squared sine-bell in the t_3 dimension, truncated at 1% at the end of the FID, and with a untruncated 90°-shifted squared sine-bell in the t_2 dimension after mirror-image linear prediction was used to extend the data along t_2 to 100*. The t_1 dimension was apodized with an untruncated 90°-shifted squared sine-bell after the data were extended to 54* by using mirror-image linear prediction. Data were zero-filled such that the digital resolutions were 15.9 (F_1), 44.0 (F_2), and 5.3 Hz (F_3).

The CBCANH spectrum (*43*) was recorded as a 33* × 60* × 512* 3D matrix with acquisition times of 21.6 (t_1, ^{15}N), 7.1 (t_2, $^{13}C^{\alpha,\beta}$), and 63.5 ms (t_3, $^1H^N$). The total acquisition time was 73.7 h. Acquired data were processed similarly to the CBCA(CO)NH and were zero-filled to yield digital resolutions of 15.9 (F_1), 44.0 (F_2), and 5.3 Hz (F_3).

The HBHA(CO)NH spectrum (*44*) was recorded as a 35* × 62* × 512* 3D matrix with acquisition times of 23.0 (t_1, ^{15}N), 15.5 (t_2, $^1H^{\alpha,\beta}$), and 63.5 ms (t_3, $^1H^N$). The total acquisition time was 42.8 h. Acquired data were processed similarly to the CBCA(CO)NH and were zero-filled to yield digital resolutions of 15.9 (F_1), 20.8 (F_2), and 5.3 Hz (F_3).

The HNCO spectrum (*45*) was recorded as a 39* × 60* × 512* 3D matrix with acquisition times of 25.6 (t_1, ^{15}N), 30.0 (t_2, $^{13}C'$), and 63.5 ms (t_3, $^1H^N$). The total acquisition time was 44.3 h. Acquired data were apodized with a 90°-shifted squared sine-bell in the t_3 dimension, truncated at 1%, and with an untruncated 90°-shifted squared sine-bell in the t_2 dimension after forward−backward linear prediction (8 coefficients) (*41*) was used to extend the data to 100*. The t_1 dimension was apodized with an untruncated 90°-shifted squared sine-bell after the data were extended to 63* by using mirror-image linear prediction (8 coefficients). Data were zero-filled to yield digital resolutions of 15.9 (F_1), 10.4 (F_2), and 5.3 Hz (F_3).

The ^{13}C-separated NOESY spectrum (*46*) was recorded as a 32* × 128* × 512* 3D matrix with acquisition times of 10.6 (t_1, ^{13}C), 23.7 (t_2, ^{1}H), and 31.7 ms (t_3, ^{1}H). The total acquisition time was 43.5 h. Acquired data were apodized with a 90°-shifted squared sine-bell in the t_3 dimension, truncated at 1%, and with a 90°-shifted sine-bell in the t_2 dimension, truncated at 7%. The t_1 dimension was apodized with a 90°-shifted sine-bell, truncated at 7%. Data were zero-filled such that the digital resolutions were 31.4 (F_1), 14.1 (F_2), and 10.5 Hz (F_3).

The ^{15}N-separated NOESY spectrum (*47*, *48*) was recorded as a 32* × 128* × 512* 3D matrix with acquisition times of 18.8 (t_1, ^{15}N), 21.3 (t_2, ^{1}H), and 67.4 ms (t_3, $^1H^N$). The total acquisition time was 98.8 h. Acquired data were apodized with a 90°-shifted squared sine-bell in the t_3 dimension, truncated at 1%, and with a 90°-shifted sine-bell in the t_2 dimension, truncated at 7%. The t_1 dimension was apodized with a 90°-shifted sine-bell, truncated at 7%. Data were zero-filled such that the digital resolutions were 17.7 (F_1), 15.6 (F_2), and 7.4 Hz (F_3).

The ^{15}N-separated HOHAHA spectrum was recorded as a 30* × 128* × 512* 3D matrix with acquisition times of 17.6 (t_1, ^{15}N), 21.3 (t_2, ^{1}H), and 50.5 ms (t_3, $^1H^N$). The total acquisition time was 40.4 h. The dipsi-2rc was used as the isotropic mixing sequence (*49*). Acquired data were apodized with a 90°-shifted squared sine-bell in the t_3 dimension, truncated at 1%, and with a 90°-shifted sine-bell in the t_2 dimension, truncated at 7%. The t_1 dimension was apodized with an untruncated 90°-shifted squared sine-bell after the data were extended to 50* by using mirror-image linear prediction. Data were zero-filled such that the digital resolutions were 26.6 (F_1), 23.4 (F_2), and 7.4 Hz (F_3).

The HNHA spectrum (*50*, *51*), for measurement of $^3J_{HNH\alpha}$, was recorded as a 58* × 70* × 512* 3D matrix with acquisition times of 38.0 (t_1, ^{15}N), 17.5 (t_2, ^{1}H), and 63.5 ms (t_3, $^1H^N$). The total acquisition time was 35.9 h. Acquired data were apodized with a 90°-shifted squared sine-bell in the t_3 dimension, truncated at 1% at the end of the free induction decay (FID), and with a 90°-shifted sine-bell in the t_2 dimension, truncated at 7%. The t_1 dimension was apodized with an untruncated 90°-shifted squared sine-bell after the data were extended to 98* by using mirror-image linear prediction. Data were zero-filled such that the digital resolutions were 11.9 (F_1), 15.6 (F_2), and 7.9 Hz (F_3). Correction of measured J values for $^1H^\alpha$ flip rates used a selective $^1H^\alpha$ T_1 value of 240 ms (*52*) for all residues.

A set of eight 2D constant-time HMQC J spectra (*51*, *52*), for measurement of $^3J_{HNH\alpha}$, were collected with dephasing periods of 45, 60, 80, 100, 120, 140, 160, 170, and 200 ms. The acquired data matrices contain 38*, 57*, 82*, 107*, 132*, 157*, 195*, and 232* complex points in the t_1 dimension and 512* in the t_2 dimension. These correspond to t_1 acquisition times of 30.4, 45.6, 65.6, 85.6, 105.6, 125.6, 156.0, and 185.6 ms and a t_2 acquisition time of 63.5 ms. Duration of the experiments was 0.7, 1.1, 1.5, 2.0, 2.5, 3.1, 4.0, and 4.9 h, respectively. Mirror-image linear prediction was used to double the number of points in the t_1 time domain, and then it was apodized with an untruncated 90°-shifted squared sine-bell. The t_2 dimension was apodized with a 90°-shifted squared sine-bell, truncated at 1%. All spectra were zero-filled to a final digital resolution of 2.4 (F_1) and 5.2 Hz (F_2). J values were obtained by fitting the peak intensities as a function of the dephasing period as described previously (*51*, *52*), with a selective $^1H^\alpha$ T_1 value of 240 ms for all residues. The pairwise root-mean-square difference between the $^3J_{HNH\alpha}$ values as determined from the ct-HMQC J and HNHA experiments was 0.3 Hz. There was negligible systematic difference between the two sets of J values.

H^N Exchange Experiment. The H^N exchange experiments were carried out on an ^{15}N-labeled vMIP-II sample lyophilized from an H_2O solution containing sodium phosphate, pH 2.5 (such that the final sample concentration would be 10 mM sodium phosphate upon rehydration with D_2O). The lyophilized protein was rehydrated with ice-cold D_2O and was added to the NMR tube on ice. The sample was then inserted in a probe, preequilibrated at 25 °C, and allowed to equilibrate for 3.5 min. The probe was then tuned and the field was shimmed. A two-scan HSQC with H_2O flip-back pulses (*40*) was started 5.5 min after the sample was inserted into the probe. Eight-scan HSQC experiments were started at 10.9 min and 1.03, 1.74, 4.21, 17.43, and 29.56 h after the sample was inserted into the probe. The two-scan HSQC lasted 5.4 min, and each eight-scan HSQC spectra took 50.7 min to acquire. All HSQC data for the exchange experiments were collected as 64* × 512* matrixes in the t_1 and t_2 time domains. Acquisition times were 51.2 (t_1) and 73.1 ms (t_2).

The data were apodized with a 90°-shifted squared sine-bell, truncated at 1%, in the t_2 dimension. The t_1 time domain was extended to 104* by mirror-image linear prediction, prior to apodization with an untruncated 90°-shifted squared sine-bell function. Data were zero-filled to 3.3 (t_1) and 4.6 Hz (t_2).

Relaxation Measurements. ^{15}N T_1, T_2, and ^{15}N{$-$H^N} *NOE* values were determined for 0.8 mM vMIP-II, from two-dimensional spectra collected using pulse sequences described previously by Kay et al. (*53*), Tjandra et al. (*54*), Grzesiek and Bax (*40*), and Farrow et al. (*55*). All spectra were collected as 160* × 512* data matrixes in the t_1 and t_2 dimensions, with acquisition times of 94.1 (t_1) and 64.0 ms (t_2). The ^{15}N T_1 data were collected with ^{15}N delays of 0.02, 0.1, 0.12, 0.18, 0.25, 0.36, 0.52, 0.76, 1.00, and 1.25 s. T_2 data were collected using ^{15}N delays of 32, 48, 64, 80, 96, 128, 144, 160, 192, and 240 ms. Two spectra were collected for each ^{15}N{$-$H} *NOE* data set, one with presaturation of ^{1}H^N (*NOE* spectrum) and one without (reference spectrum). A relaxation delay of 5 s was used for the reference spectrum, and a 2 s relaxation delay was followed by a 3 s ^{1}H^N presaturation period for the *NOE* spectrum. ^{15}N T_1, T_2, and ^{15}N{$-$H} *NOE* data sets were collected twice, several days apart. The time points for the T_1 and T_2 data sets were randomized differently for each set, and interleaved such that all 10 ^{15}N delays were sampled at each t_1 period, to minimize spectrometer drift effects. Acquisition times were 23.0, 18.3, and 31.5 h for each T_1, T_2, and *NOE* data set, respectively. All spectra were apodized in the t_2 dimension with a 90°-shifted squared sine-bell, truncated at 1%. The t_1 time domain was apodized with a 90°-shifted sine-bell, truncated at 7%. The spectra were zero-filled to 3.3 (t_1) and 5.2 Hz (t_2). The measured ^{15}N{$-$H} *NOE* values were mathematically corrected by a small factor for incomplete ^{1}H^N recovery (*40*).

RESULTS

^{15}N T_1, T_2, and ^{15}N{$-H^N$} NOE data. ^{15}N T_1 and T_2 and ^{15}N{$-$H} *NOE* values for 66 residues could be determined out of a total of 74 for vMIP-II. Six unobservable residues were prolines (Pro11, Pro22, Pro24, Pro33, Pro41, and Pro70), the resonance of Cys15 was too weak to be observed, and the chemical shifts of Leu23 were not unambiguously identified due its position between two proline residues. Experiments to measure ^{15}N T_1, T_2, and ^{15}N{$-$H} *NOE* were repeated twice, several days apart. The pairwise rms differences between the two sets of measurements were 2.2%, 2.8%, and 6.4% of the averaged ^{15}N T_1, T_2, and ^{15}N{$-$H} *NOE* values, respectively, indicating random errors of 1.1% (T_1), 1.4% (T_2), and 3.2% (*NOE*) in the averaged values. The uncertainties in the T_1 and T_2 values, as determined from fitting of the decay curves, were also 1.1% and 1.4%, respectively. It was recently shown that, due to rf heating effects caused by the large number of pulses in a ^{15}N T_2 experiment, it is possible to obtain precise but inaccurate ^{15}N T_2 values on a sample with a 100 mM salt concentration if the relaxation delay is less than approximately 2.5 s (*56*). As our salt concentration was only 10 mM, rf heating effects were less serious (*57*), and our relaxation delay was 1 s.

An estimate of the rotational correlation time was obtained from ^{15}N T_1/T_2 ratios. Provided residues experiencing internal motions occurring on a time scale slower than 100 ps and/or conformational exchange dynamics are absent, the T_1/T_2 ratio is a good measure of the global rotational correlation time, τ_c (*55*, *58*−*60*). Residues experiencing internal motions with internal correlation times longer than approximately 100 ps were identified by ^{15}N{$-$H} *NOE* values < 0.65 (*58*). Such residues were excluded from this initial T_1/T_2 analysis. Residues were identified as undergoing conformational exchange if they satisfied the following equation (*54*, *60*):

$$(\langle T_2\rangle - T_{2,n})/\langle T_2\rangle - (\langle T_1\rangle - T_{1,n})/\langle T_1\rangle > 1.5\mathrm{SD} \quad (1)$$

$\langle T_2\rangle$ and $\langle T_1\rangle$ are the average ^{15}N T_2 and T_1 values, respectively; $T_{2,n}$ and $T_{1,n}$ are the T_2 and T_1 values of residue n; and SD is the standard deviation of $(\langle T_2\rangle - T_{2,n})/\langle T_2\rangle - (\langle T_1\rangle - T_{1,n})/\langle T_1\rangle$, excluding residues with a ^{15}N{$-$H} *NOE* < 0.65. Of the 66 residues where a ^{15}N{$-$H} *NOE* value could be calculated, 25 (Gly1−Arg10, Asp12−Cys14, Gly17, Tyr18, Lys20, Arg21, Leu37, Ser39, Lys40, Gly42, Gly50, Leu69, Ala73, and Arg74) had values less than 0.65, and of the remaining 40 residues, six (Asn25−Leu27, Asn36, Cys38, and Ala55) were identified as possibly experiencing conformational exchange dynamics as indicated from eq 1. These residues were not included in the τ_c calculation using the T_1/T_2 ratio. The average T_1/T_2 ratio from the remaining 34 residues was 3.2 ± 0.3. Shown in Figure 1 are the ^{15}N T_1, T_2, and ^{15}N{$-$H} *NOE* values as a function of residue. Horizontal dashed lines are drawn at the positions of the average values of T_1 (485 ± 30 ms), T_2 (152 ± 13 ms), and T_1/T_2 (3.2 ± 0.3), calculated from these 34 residues. The dashed horizontal line in the graph of the ^{15}N{$-$H} *NOE* values is placed at 0.65. The open ovals represent the residues with ^{15}N{$-$H} *NOE* < 0.65, the shaded boxes represent residues whose ^{15}N{$-$H} *NOE* ≥ 0.65 but that were identified by eq 1 as experiencing conformational exchange, and the solid ovals represent the remaining 34 residues that were used in the initial τ_c estimate (^{15}N{$-$H} *NOE* ≥ 0.65 and did not satisfy eq 1).

An estimate of the rotational correlation time, τ_c, was obtained from minimizing the following equation:

$$E = \sum_n (T_{1,n}{}^{\mathrm{obs}}/T_{2,n}{}^{\mathrm{obs}} - T_1{}^{\mathrm{calc}}/T_2{}^{\mathrm{calc}})^2/\Delta^2 \quad (2)$$

$T_{1,n}{}^{\mathrm{obs}}$ and $T_{2,n}{}^{\mathrm{obs}}$ are the experimentally determined ^{15}N relaxation times, $T_1{}^{\mathrm{calc}}$ and $T_2{}^{\mathrm{calc}}$ are the calculated ^{15}N relaxation times, assuming isotropic tumbling and no internal dynamics, Δ is the estimated uncertainty in the $T_1{}^{\mathrm{obs}}/T_2{}^{\mathrm{obs}}$ ratio, and the summation is for the 34 residues. The equations for $T_1{}^{\mathrm{calc}}$ and $T_2{}^{\mathrm{calc}}$ are well-known and are given elsewhere (*55*, *58*, *59*). The spectral density used for $T_1{}^{\mathrm{calc}}$ and $T_2{}^{\mathrm{calc}}$ is given by $J(\omega) = S^2\,\tau_c/(1 + \omega^2\tau_c{}^2) + (1 - S^2)\tau/(1 + \omega^2\tau^2)$, where $\tau = \tau_e\tau_c/(\tau_e + \tau_c)$, and $\tau_e \ll \tau_c$ (*61*). S^2 is the order parameter describing the spatial restriction of the fast internal motion and τ_e is the internal motion correlation time. As residues experiencing only extremely fast internal dynamics are used in the determination of τ_c, the T_1/T_2 ratio is insensitive to both S^2 and τ_e. Therefore, for the minimization of eq 2 using the subset of 34 residues, S^2 was set to 1, τ_e was set to 0, and a one-dimensional grid search as a function of τ_c was performed. The τ_c was 4.7 ns, as determined from eq 2, and $E = 17$. The uncertainty in τ_c was estimated by repeatedly deleting 20% of the residues used in eq 2 followed by recalculation of τ_c. The difference between the maximum

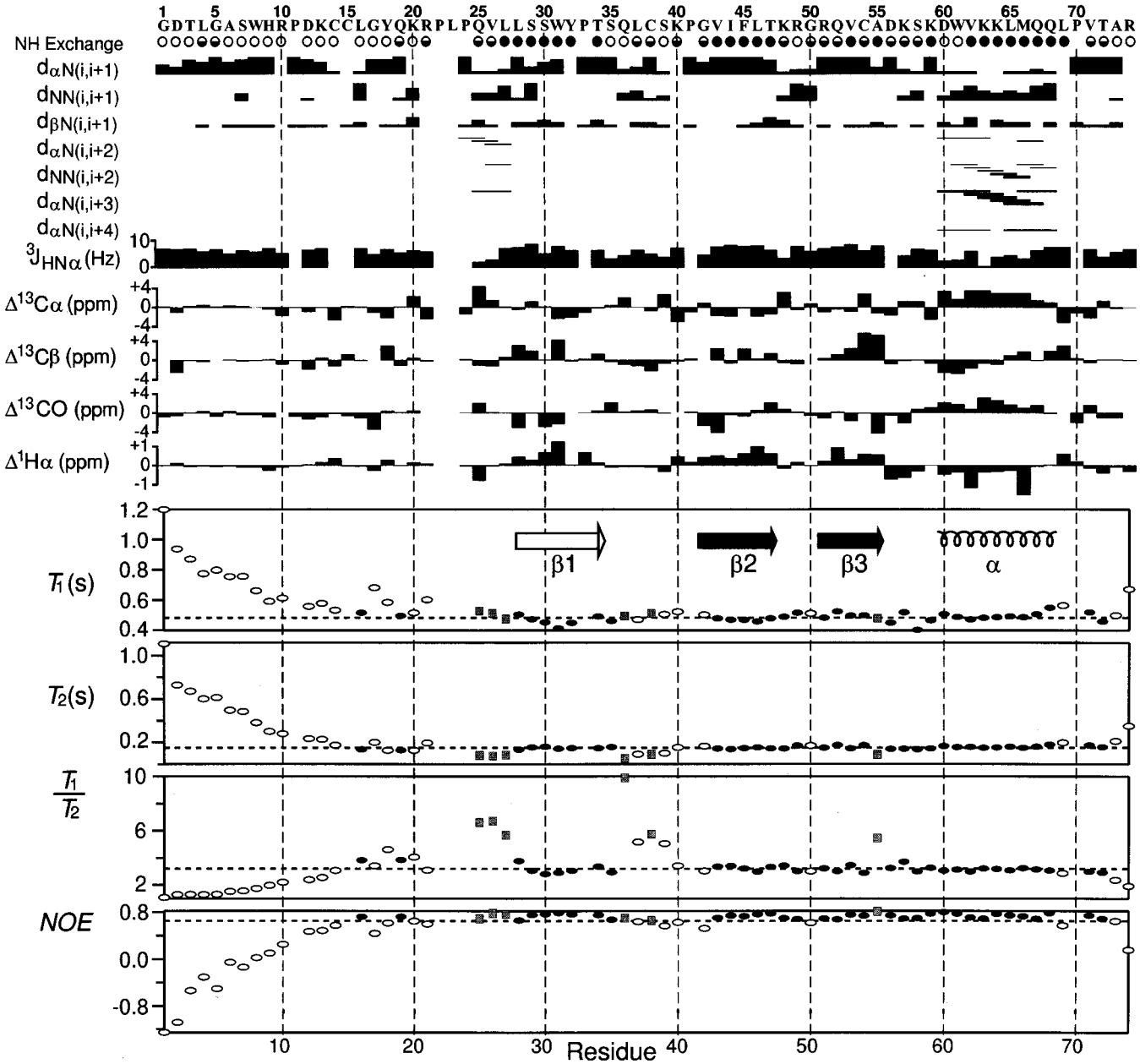

FIGURE 1: Diagram of NMR data of vMIP-II, as a function of residue. Shown are H^N exchange data, sequential and medium-range $^1H-^1H$ *NOE* distances, $^3J_{HNH\alpha}$ values, deviations from random coil chemical shift values of $^{13}C^\alpha$, $^{13}C^\beta$, $^{13}C'$, and $^1H^\alpha$, and ^{15}N T_1, T_2, T_1/T_2, and $^{15}N\{-H\}$ *NOE* values. The H^N exchange data are represented by circles. Open circles represent amides whose exchange rates are much faster than the dead time of the experiment (5.5 min) and therefore were not observable in the first spectrum. Solid circles mark residues whose amides were present 17.4 h after insertion of the sample into the probe. A half-filled circle marks residues whose ^{15}N, $^1H^N$ HSQC cross-peak was observable between 5.5 min and 4.2 h after the sample was inserted into the probe but was not seen in the spectrum measured at 17.4 h. Sequential H−H distances, $d_{\alpha N}(i, i+1)$, $d_{NN}(i, i+1)$, and $d_{\beta N}(i, i+1)$, are represented on an arbitrary vertical scale as filled black boxes. Medium-range H−H distances, $d_{\alpha N}(i, i+2)$, $d_{NN}(i, i+2)$, and $d_{\alpha N}(i, i+4)$, are shown as black lines, and the line thickness reflects the relative H−H *NOE* cross-peak intensity. Three-bond $^3J_{HNH\alpha}$ values are the average of values obtained from the 3D HNHA spectrum and the HNHA ct-HMQC *J* experiment (*50*, *51*). The random coil chemical shifts are relative to DSS (*39*) and the vertical scale is in parts per million. The ^{15}N T_1, T_2, and $^{15}N\{-H\}$ *NOE* values were measured as described in the text. Filled ovals represent residues whose $^{15}N\{-H\}$ *NOE* ≥ 0.65 and whose relaxation times did not satisfy eq 1, shaded boxes represent residues whose $^{15}N\{-H\}$ *NOE* ≥ 0.65 but did satisfy eq 1, and open ovals represent residues whose $^{15}N\{-H\}$ *NOE* < 0.65. The horizontal dashed lines in the graphs of T_1, T_2, and T_1/T_2 represent the average of the values for those residues whose $^{15}N\{-H\}$ *NOE* was greater than or equal to 0.65. The horizontal dashed line in the graph of the *NOE* values is at 0.65. Horizontal arrows delineate regions of β-strands, as deduced from secondary chemical shift data. The unfilled arrow for $\beta 1$ reflects the fact that while chemical shift data and some *NOE* data suggest a β strand in this region, the presence of a proline at position 33 and H^N to $H^N(i+1)$ *NOE*s from residues 28−30 are inconsistent with β-strand secondary structure.

and minimum values in the τ_c values after 200 such iterations was 0.2 ns.

Rotational Diffusion Anisotropy. To estimate the magnitude of rotational diffusion anisotropy, $r = D_{||}/D_\perp$, the equation presented by Schurr et al. (*62*) was used: $r = (5R' - 2)/(4 - R')$ (*62*), where R' is the ratio of the longest and the shortest best-fit residue-specific τ_c. ^{15}N relaxation data were fit by using the simple isotropic spectral density function to calculate an apparent, best-fit τ_c and optimal S^2 and τ_e values for each low-mobility residue. Schurr et al.

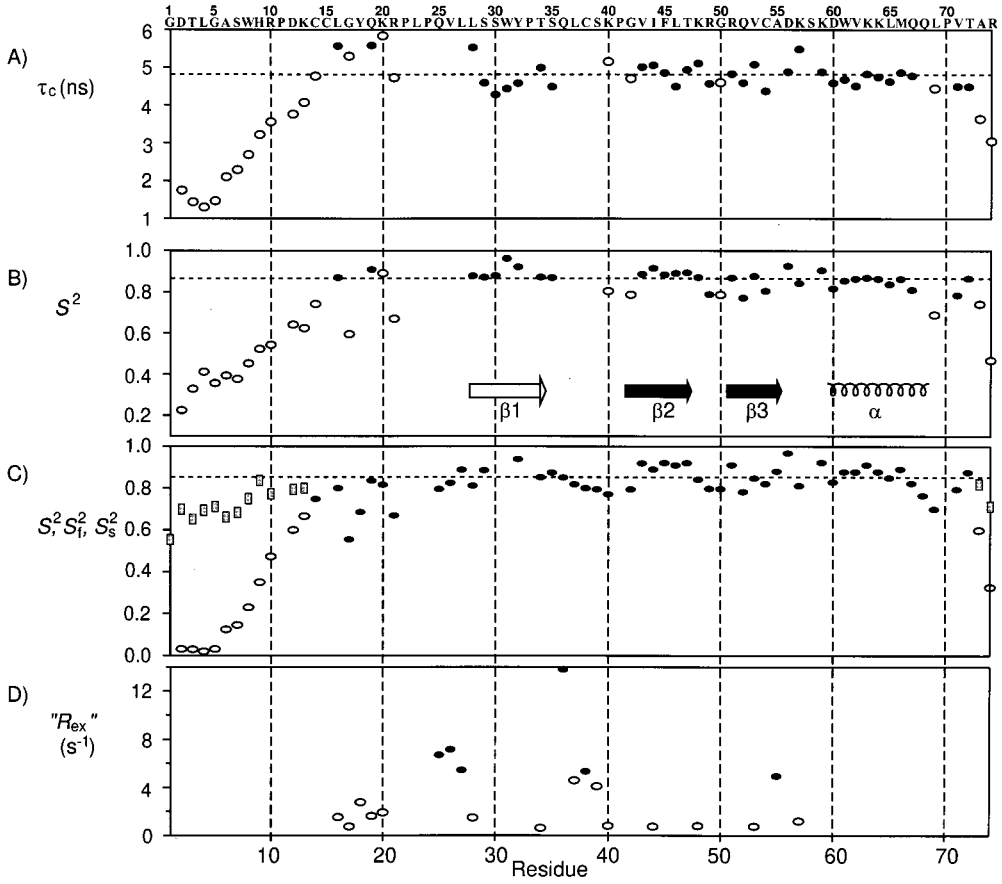

FIGURE 2: Internal dynamics graphs of apparent τ_c, S^2, S_f^2, S_s^2, and "R_{ex}" values calculated from experimental ^{15}N T_1, T_2, and $^{15}N\{-H^N\}$ *NOE* values as explained in the text. (A) Apparent τ_c values obtained by finding an optimal τ_c for each residue, in addition to S^2 and τ_e, using eq 3, assuming isotropic tumbling, and using the simple model-free model spectral density function (*61*). Filled ovals represent the residues (33 total) whose apparent τ_c values were used to calculate the average τ_c of 4.7 ± 0.3 ns. The 33 residues had $^{15}N\{-H\}$ *NOE* ≥ 0.65 and did not appear to experience significant conformation exchange as indicated by eq 1. The horizontal dashed line is placed at 4.7 ns. Open ovals represent the remaining residues whose relaxation parameters could be fit to within 95% confidence limits. (B) S^2 values determined by the identical method described for panel A. Filled and unfilled ovals follow the same criteria as in panel A. The horizontal dashed line is placed at 0.83, the average of the values of the 33 residues whose individual S^2 values are shown as filled ovals. (C) S^2 (models I and II) and S_f^2 and S_s^2 (model III). Model I used the simple model-free model spectral density function (*61*), $J(\omega) = S^2\,\tau_c/(1 + \omega^2\tau_c^2) + (1 - S^2)\tau/(1 + \omega^2\tau^2)$, as explained in the text. Model II used the same spectral density function but included an extra relaxation term in the equation describing ^{15}N T_2 relaxation: $T_2^{-1} = T_{2,DD}^{-1} + T_{2,CSA}^{-1} + R_{ex}$". Model III used the spectral density equation $J(\omega) = S_f^2S_s^2\tau_c/(1 + \omega^2\tau_c^2) + (S_f^2 - S_f^2S_s^2)\tau/(1 + \omega^2\tau^2)$ (*66*, *67*), which is defined in the text. Filled ovals represent residues whose relaxation data could be fit to within 95% confidence limits by either model I or II. Open ovals and shaded boxes represent, respectively, the S_s^2 and S_f^2 values of residues that could only be fit with model III. The horizontal dashed line represents the average of the S^2 (models I and II) and S_f^2 (model III) values, 0.82, from residues 14−74. (D) "R_{ex}" values shown in reciprocal seconds. The filled ovals represent the six residues that were indicated by eq 1 to experience conformational exchange dynamics. The unfilled ovals are those residues that also required a "R_{ex}" term but either had a $^{15}N\{-H\} < 0.65$ or were missed by eq 1.

(*62*) have demonstrated that if the diffusion tensor of the protein is axially symmetric, the diffusion anisotropy, *r*, can be estimated from the shortest and longest best-fit τ_c values, where it is assumed that residues with the shortest and longest τ_c values have N−H bonds oriented at 90° and 0° relative to the principal diffusion axis, respectively. In this case, the following equation was minimized on a residue-by-residue basis by using a grid search:

$$E = (T_1^{calc} - T_1^{obs})^2/\sigma_{T1}^2 + (T_2^{calc} - T_2^{obs})^2/\sigma_{T2}^2 + (NOE^{calc} - NOE^{obs})^2/\sigma_{NOE}^2 \quad (3)$$

σ_{T1}, σ_{T2}, and σ_{NOE} are the estimated standard deviations in T_1^{obs}, T_2^{obs}, and NOE^{obs} for a given residue. Starting with the same 34 rigid residues as above, only residue Tyr18 could not be fit within 95% confidence limits and was therefore eliminated. The resulting averages are $\tau_c = 4.7 \pm 0.3$ ns and $S^2 = 0.87 \pm 0.04$. Residue Trp31 had the longest τ_e value (595 ps), and discounting this outlier, the average $\tau_e = 44 \pm 35$ ps. Shown in Figure 2A,B are the residue-specific, best-fit τ_c and S^2 values obtained by minimizing eq 3. The dashed horizontal lines show the level of the average values for τ_c and S^2, as calculated for the 33 residues. The values for these 33 residues are shown as solid ovals and those of the other residues are drawn as open ovals. Of these 33 residues, four residues (Leu16, Asn19, Leu28, and Lys57) possess the longest τ_c values, 5.35 ± 0.05 ns, and eight residues (Ser30, Trp31, Ser35, Leu46, Cys54, Val62, Val71, and Thr72) possess the shortest τ_c values, 4.3 ± 0.1 ns. The above τ_c values for vMIP-II gave a value of $r = 1.5 \pm 0.1$. This approach can give a slightly overestimated *r* value (*62*, *63*). However, statistically, for a uniform distribution of N−H vectors in space, the probability of finding an N−H bond with an angle of 0° relative to the principal diffusion axis is

low (probability follows a sin θ distribution) (*64*). The longest τ_c value of 5.35 ns is consequently most likely an underestimate, thereby yielding an underestimated r value. The extent to which these two opposite effects cancel out to produce the final r value was not explored here, however.

Backbone Dynamics. In an effort to gain additional insight on the backbone dynamics of vMIP-II, some conservative modeling of backbone dynamics was performed. This time, τ_c was fixed at 4.7 ns for all residues, isotropic tumbling was assumed, and the three models used during the minimization of eq 3, in order of increasing complexity, were (I) fast internal motions of restricted amplitude (*65*); (II) same as model I but with the addition of slow conformational exchange to account for such effects on T_2 (*55*, *59*); and (III) the simultaneous presence of both fast and intermediate time scale internal motions (*66*, *67*). The spectral density for model I is given by $J(\omega) = S^2\,\tau_c/(1 + \omega^2\tau_c^2) + (1 - S^2)\tau/(1 + \omega^2\tau^2)$, where $\tau = \tau_e\tau_c/(\tau_e + \tau_c)$, and $\tau_e \ll \tau_c$. S^2 is the order parameter describing the spatial restriction of the fast internal motion and τ_e is the internal motion correlation time. The spectral density functions for model II are the same as for model I, and conformational exchange is accounted for by the addition of the term "R_{ex}" to the equation for T_2, $T_2^{-1} = T_{2,DD}^{-1} + T_{2,CSA}^{-1} +$ "R_{ex}" [quotes are added here as a reminder that a putative R_{ex} exchange term can sometimes be explained by anisotropic tumbling rather than by actual conformational exchange (*54*, *62*, *63*)]. The spectral density function for model III is given by $J(\omega) = S_f^2S_s^2\,\tau_c/(1 + \omega^2\tau_c^2) + (S_f^2 - S_f^2S_s^2)\tau/(1 + \omega^2\tau^2)$, where $\tau = \tau_s\tau_c/(\tau_s + \tau_c)$, $\tau_c > \tau_s$, S_f^2 is the order parameter for the fast internal motion, S_s^2 is the order parameter for the intermediate time scale internal motion, and τ_s is the internal correlation time describing intermediate time scale motions. Determination of the model most consistent with the ^{15}N relaxation data for a particular residue was carried out by minimizing eq 3. Minimization of eq 3 was achieved by using a grid search of the internal dynamics parameters for each model. Residues whose T_1^{obs}, T_2^{obs}, and NOE^{obs} values could be fit within 95% confidence limits by using model I were assigned that model, and those that could not were then fit with model II. Those that could not be adequately described by either model I or II were finally fit with model III. Out of a total of 64 residues that were modeled, 30 had ^{15}N relaxation parameters that could be fit within 95% confidence limits by model I (Cys14, Arg21, Ser29, Tyr32, Ser35, Gly42, Val43, Phe45−Thr47, Arg49−Gln52, Cys54, Asp56, Ser58−Leu69, Val71, and Thr72), 20 could not be fit by the simple model but needed an "R_{ex}" term added to the equation for T_2 (*68*) (Leu16−Lys20, Gln25−Leu28, Thr34, Gln36−Lys40, Ile44, Lys48, Val53, Ala55, and Lys57), and the backbone dynamics of 14 residues required two time scales to adequately describe the internal dynamics, i.e., could be fit only by model III, the extended model-free model (*67*) (Gly1−Arg10, Asp12, Lys13, Ala73, and Arg74). The ^{15}N T_1^{obs}, T_2^{obs}, and ^{15}N{−H} NOE^{obs} values of Ser30 and Trp31 could not be adequately approximated by any of the three models. The results are shown in Figure 2C,D. The solid ovals in Figure 2C represent the S^2 values of those residues that could be fit by either model I or II. The open ovals and shaded boxes represent the S_s^2 and S_f^2 values, respectively, of those residues fit with model III. Figure 2D illustrates the potential conformational exchange occurring in vMIP-II. The filled ovals in Figure 2D are those residues that were indicated by eq 1 to undergo conformational exchange dynamics. The open ovals required a "R_{ex}" term in the T_2 equation for an adequate fit to the ^{15}N relaxation data but did not satisfy eq 1. It has been reported by several investigators that neglect of moderate levels of rotational anisotropy has little effect on S^2 values but can erroneously suggest the presence of conformational exchange for a given residue when, in fact, none exists (*54*, *56*, *60*, *62*, *63*). vMIP-II residues that are actually experiencing significant conformational exchange dynamics can be identified by considering T_1/T_2 ratios, the measured anisotropy, $r = 1.5 \pm 0.1$, and the experimental correlation time, $\tau_c = 4.7 \pm 0.3$ ns. Given this anisotropy, the range of T_1/T_2 ratios is expected to be 4.6 if the polar angle, θ, is 0° and 2.8 if $\theta = 90°$. Those residues with experimental ratios that are larger than 4.6 are most likely actually experiencing significant conformational exchange dynamics. Recall that 20 residues required an "R_{ex}" term (model II) for an adequate fit to their relaxation data. Out of these, eight were found to have ratios greater than 4.6. Six of these residues are the same ones that were previously identified as experiencing conformational exchange, according to eq 1. Two additional residues, Leu37 and Ser39, have ratios of 5.2 and 5.0, respectively, and are therefore most likely experiencing conformational exchange dynamics as well. The remaining 12 R_{ex} residues, however, have T_1/T_2 ratios that are between 2.8 and 4.6, and therefore may or may not be experiencing conformational exchange.

Secondary Structure of υMIP-II. To interpret dynamics data in the context of structure, a structural analysis of vMIP-II was carried out. The 2D HSQC spectrum for vMIP-II is shown in Figure 3 as a demonstration of the spectral quality. Most chemokines aggregate at pH values near neutrality, and NMR studies of these proteins are usually carried out under acidic conditions (*11*, *13*, *16*). Among chemokines whose structure has been determined, vMIP-II shares the highest amino acid identity with MIP-1β, the structure of which was determined at pH 2.5. Therefore, the spectra of vMIP-II were uniformly measured at pH 2.5. A control HSQC spectrum measured at pH 5.1 was nearly identical to the spectrum measured at pH 2.5, with significant changes in chemical shift in only six charged residues and two amino acids adjacent to charged residues.[2] As it was recently shown that chemical shifts of dimer interface residues in MIP-1β are sensitive to dimerization (*69*), this spectral similarity suggests (but does not prove) that no significant difference in structure or dimer type exists between pH 2.5 and 5.1. Location of the secondary structural elements of vMIP-II was accomplished from analysis of backbone chemical shifts and three-bond H−H J values. The tertiary fold of vMIP-II was determined from analysis of H−H NOESY data in ^{13}C- and ^{15}N-separated 3D spectra.

Backbone chemical shifts ($^1H^N$, ^{15}N, $^{13}C'$, $^{13}C^\alpha$, $^{13}C^\beta$, $^1H^\alpha$, and $^1H^\beta$) were determined from a series of 3D heteronuclear NMR spectra [HNCO, CBCA(CO)NH, CBCANH, and HBHA(CO)NH] (*70*). These values are reported in Table

[2] A comparison of the HSQC spectrum measured at pH 5.1 and that measured at pH 2.5 shows eight resonances with a $^1H^N$ chemical shift change greater than 0.05 ppm or a ^{15}N chemical shift change of more than 0.5 ppm: Asp2, Asp12, Lys13, Lys57, Ser58, Asp60, Trp61, and Arg74.

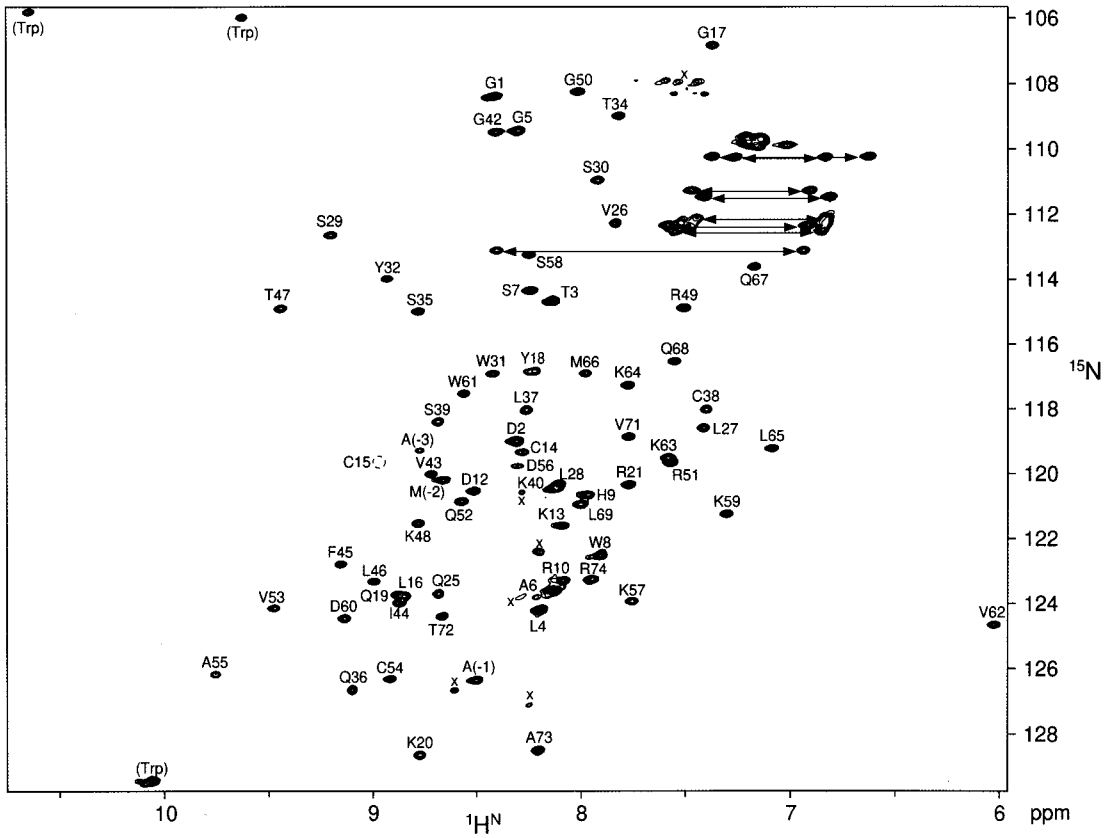

FIGURE 3: Two-dimensional $^1H-^{15}N$ HSQC [with water flip-back (*40*)] spectrum of vMIP-II, uniformly labeled with ^{15}N (>95%), recorded at 600 MHz. Cross-peaks connected by arrows correspond to Gln side-chain NH_2 groups. Cross-peaks marked with x are impurities.

S1 of the Supporting Information. Several groups have carefully studied the relationship between chemical shift values and the secondary structure of a protein (*71*−*74*) and have shown that the chemical shift values of several residues in combination can be used to predict with some confidence the secondary structure of the protein. From these data, vMIP-II evidently has a β-strand from Leu28 to Thr34 (β1); a β-strand from Gly42 to Thr47 (β2), and a β-strand from Arg51 to Ala55 (β3). In addition, an α-helix is present near the C-terminus of the protein, involving residues Asp60−Gln68 (see Figure 1). The N-terminal segment of vMIP-II, which extends from Gly1 to about residue Arg21, does not appear to have a region of consistent secondary structure as judged by chemical shift analysis and ^{15}N relaxation data (vide supra).

Other data can be used in combination with chemical shift data to provide further structural information. The $^3J_{HNH\alpha}$ coupling constant correlates with the backbone ϕ angle of a protein (*50*, *75*) and as such can also indicate secondary structure. A large coupling constant indicates a ϕ angle consistent with a β-strand, while a small coupling constant indicates a ϕ angle consistent with an α-helix. Figure 1 shows a graphical representation of the $^3J_{HNH\alpha}$ coupling constants (averaged from HNHA and ct-HMQC *J* data) that were obtained from analysis of vMIP-II. These values are consistent with the chemical shift data, particularly in the confirmation of a C-terminal α-helix.

The 3D ^{15}N-separated NOESY spectrum provides a direct indication of secondary structure and is particularly effective in delineating the bounds of an α-helix. The H−H *NOE* contacts depicted in Figure 1 clearly indicate the presence both of an α-helix from residues Asp60 to Gln68 and the presence of a turn from residues Pro24 to Leu27. In addition, while the chemical shift data indicate that the first β-strand of vMIP-II begins at residue Leu28, the NOESY data show $H^N(i)$ to $H^N(i + 1)$ connections until residue Ser30, which is generally inconsistent with a β-strand.

The amide exchange lifetime of the backbone of vMIP-II was also measured and is shown in Figure 1. This type of experiment provides valuable information about the secondary and tertiary structure of a protein, as amide hydrogens involved in H-bonding and shielded from solvent will exchange more slowly than solvent-exposed amides (ref *76* and references therein). For the predicted α-helix, all but the N-terminal amide hydrogens of the helix are resistant to exchange, as expected. In addition, most of the β-strands show significant protection from hydrogen exchange, as does much of the region from Gln25 to Leu27 that is expected to contain an ordered turn. The loop regions between the secondary structural units experience more amide exchange than the secondary structural units themselves.

Both the amide exchange data and the ^{15}N-separated NOESY provide an interesting glimpse of the N-terminus of vMIP-II, which is the region that has been shown to be important for receptor activation in other chemokines (*32*−*36*). The NOESY shows many contacts between adjacent residues in the region from residue Gly1 to Lys13 but appears to have few long-range contacts. The amide exchange data show fast exchange rates for most of these early residues of the protein, except for Leu4 and Gly5. The data indicate a disordered N-terminus, with high access to solvent, followed by a region before the first β-strand that has moderate protection of some amides and experiences conformational exchange dynamics.

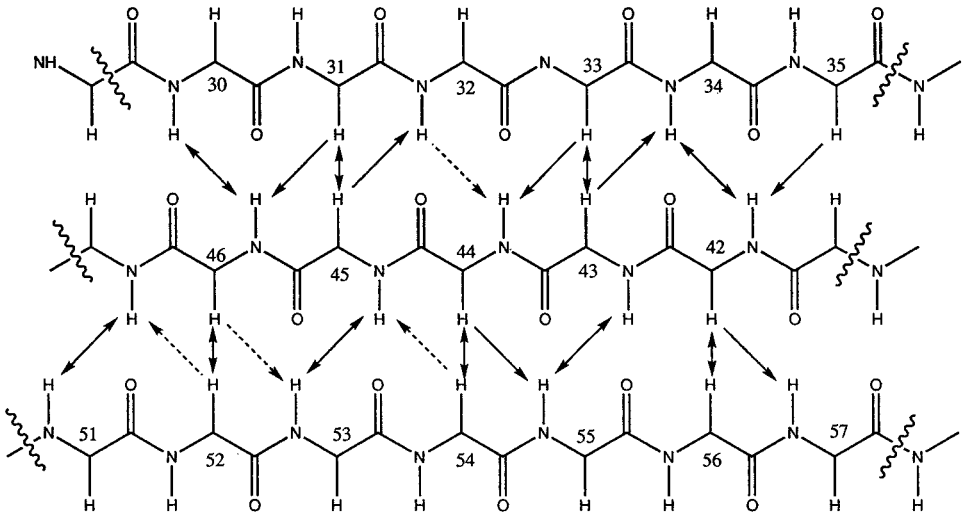

FIGURE 4: Arrangement of the antiparallel β-sheet in vMIP-II. Solid arrows indicate the presence of unambiguous H−H *NOE* cross-peaks in either the ^{15}N NOESY or the ^{13}C NOESY spectrum. A dotted arrow indicates the presence of a peak that could be assigned to the shown interaction, but whose chemical shift overlap also makes an alternative assignment possible. As noted in the text, chemical shift values indicate a β1 strand from residues 28−34, while *NOE* resonances show clear cross-strand connections beginning at residue 30.

In combination, the data accumulated in Figure 1 provide a picture of the secondary structure of vMIP-II, showing it to consist of three β-strands and a C-terminal helix, similar to other known chemokine monomeric units (*11*−*20*, *77*). However, the β1 strand may experience an unusual local structure because of its amino acid composition. Both proline and glycine have been shown to have a very low propensity to be found in β-strands (*78*), and while Gly42 of β2 may be tolerable because it is at the edge of the strand, putative strand β1 has a proline near its center at position 33. The chemical shift data indicate a β-strand for residues 28−34, while H−H *NOE* data indicate a strand that does not begin until residue Ser30 and is consistent with a continuation of this strand through residue 34. In Figure 1 we show a white arrow rather than a solid black arrow from residues 28−34 to represent a β-strand in this region that may deviate from canonical β structure. Overall, the secondary structure of vMIP-II can be described by β-strands that extend from about Ser30 to Thr34 (β1), Gly42 to Thr47 (β2), and Arg51 to Ala55 (β3). The helix in vMIP-II begins at residue Asp60 and extends to residue Gln68. Interestingly, and unlike most chemokines, the helix of vMIP-II does not extend to the end of its C-terminus, but rather is disrupted by a proline at residue 70, with the remaining four residues apparently having no defined secondary structure.

Tertiary Fold of vMIP-II. The tertiary fold of vMIP-II can be discerned from an examination of the 3D ^{15}N-separated NOESY and 3D ^{13}C-separated NOESY spectra. As shown in Figure 4, clear cross-peaks are visible between the backbone protons of the β1 strand with those of the β2 strand and between the β2 strand and the β3 strand, the pattern of which dictates the arrangement of an antiparallel β sheet. In addition, the side chains of the C-terminal helix of vMIP-II make several contacts to the β sheet in a manner analogous to the contacts made by MIP-1β (*11*), indicating similar placement of the helix with respect to the sheet. For example, Leu69 contacts Trp31, and both Met66 and Lys57 contact Val43. Overall, based on the positioning in the sequence and spatial connectivity between the secondary structural elements of vMIP-II, this protein apparently has a typical chemokine fold consisting of an N-terminal region without a consistent, obvious secondary structure, followed by an ordered turn, then a series of three antiparallel β-strands, and concluded by a C-terminal α-helix that in this case is disrupted before reaching the very C-terminus by the presence of a proline at position 70.

DISCUSSION

vMIP-II is a Kaposi's sarcoma-associated herpesvirus-encoded CC chemokine that interacts with a broad spectrum of chemokine receptors, having the unique ability to bind both CC and CXC chemokine receptors at high affinity (*30*, *31*). In conjunction with this property, vMIP-II is able to block infection by a variety of strains of HIV-1, based on the utilization by HIV strains of CCR5, CCR3, and CXCR4 as coreceptors (*29*−*31*). As there is usually a lack of cross-binding between receptors of one subfamily and chemokines of the other main subfamily, the structural characteristics of vMIP-II that allow its unusual activities are of great interest both biochemically and as a medically important model for designing anti-HIV therapeutics. The protein used in our studies is biologically active, as shown by its ability to bind the chemokine receptors CCR5 and CXCR4 (unpublished) although others report that the mature protein begins at Leu4 in our numbering system (*31*) and that the final arginine is removed.

vMIP-II Is a Monomer. As previously discussed, the multimeric state of the functional chemokine is the subject of some controversy, with most structures revealing a chemokine dimer (*11*−*20*) while biochemical evidence demonstrates the activity of some chemokine monomers (*21*−*23*). We performed ^{15}N relaxation measurements on vMIP-II and find the rotational correlation time (τ_c) of vMIP-II to be 4.7 ± 0.3 ns. For comparison, the τ_c of the wild-type MIP-1β dimer (138 residues) is 8.6 ns (*69*), while a 60 amino acid, N-terminally truncated monomeric variant of MIP-1β called MIP(9) has a τ_c of 4.5 ns (*69*). The correlation time for vMIP-II clearly indicates that it exists under our NMR conditions as a monomeric species. It is possible that solution conditions could be changed to favor dimer formation in vMIP-II, as the oligomeric state of other chemokines

has been shown to be dependent on pH (*13*) and salt conditions (*23*, *69*, *79*). In the case of MIP-1β and its mutants, the ^{15}N HSQC spectrum of the dimer is quite different than that of the monomeric form (*69*), and as such it is likely that a change in oligomeric state of vMIP-II would lead to a substantially altered ^{15}N HSQC spectrum. However, we preliminarily find that neither an increase in the pH of the NMR sample nor the addition of sodium chloride leads to a significantly altered ^{15}N HSQC spectrum for vMIP-II.

The existence of an apparently purely monomeric chemokine at high concentrations is atypical but not without precedent: the solution structure of the CC chemokine MCP-3 has been described by two groups, one of which claims that the protein is a monomer (*80*), with the other reporting a dimer under similar conditions (*15*). Similarly, the CXC chemokine SDF-1 was recently reported to be monomeric in solution (*77*), although X-ray crystal studies revealed a dimer (*81*). The rotational correlation time of a protein in solution can be a very reliable indicator of oligomeric state, particularly when a comparison can be made with other similar proteins of known oligomeric state. However, this type of determination requires the use of isotopically labeled protein and was not carried out for MCP-3 (*15*, *80*) or SDF-1 (*77*). As such, our studies are the first that rigorously determine the rotational correlation time (τ_c) of a monomeric chemokine as an indicator of multimeric state in solution.

Tertiary Fold of vMIP-II. Our investigation shows that vMIP-II has secondary structural characteristics and an overall fold similar to other known chemokines. H−H *NOE* contacts seen in the ^{15}N- and ^{13}C-separated NOESY spectra reveal that the three β-strands are arranged in an antiparallel arrangement and that the α-helix is oriented approximately perpendicular to the sheet, similar to the fold of MIP-1β. As the anisotropy of rotational diffusion was estimated to be 1.5 ± 0.1, assuming vMIP-II has an axially symmetric diffusion tensor, additional structural information can be gained from analysis of the ^{15}N T_1/T_2 ratios, provided (1) residues with internal motions slower than about 100 ps and (2) residues experiencing conformational exchange on a micro- to millisecond time scale are not included (*54*, *56*, *60*, *63*, *64*). The T_1/T_2 ratio in this case is a function of the angle (θ) the N−H bond makes with the principal axis of diffusion. Accordingly, the ^{15}N T_1/T_2 ratios of the β-strands and α-helix are 3.0 ± 0.2, 3.2 ± 0.2, 3.1 ± 0.1, and 3.1 ± 0.1 for β1, β2, β3, and the α-helix, respectively. These ^{15}N T_1/T_2 ratios are consistent with the finding from H−H *NOE* contacts that the β-strands are arranged as an antiparallel β-sheet, and the α-helix is approximately perpendicular to the β-strands. As $\tau_{c,eff} = 4.7 \pm 0.3$ ns and $r = 1.5 \pm 0.1$, a T_1/T_2 ratio of 2.8 would indicate $\theta = 90°$, while a T_1/T_2 of 4.6 would indicate $\theta = 0°$. The values around 3.0 for vMIP-II indicate that the principal axis of diffusion lies within a plane that is approximately perpendicular to the NH vectors of both the β-strands and the α-helix, an arrangement that is consistent with a typical chemokine fold.

Internal Dynamics of vMIP-II. ^{15}N T_1, T_2, and ^{15}N{−H^N} *NOE* data were used to estimate the internal dynamics of vMIP-II. These dynamics parameters correlate well to the deduced secondary structure of the protein. The order parameter S^2 (and S_f^2) provides information on the range of motion of an N−H vector on a picosecond time scale (*58*, *61*). The value can range from 0 (completely disordered) to 1 (completely rigid). These order parameters for vMIP-II are shown in Figure 2B,C and their average values, not including S_s^2 and excluding the first 13 residues, are 0.83 ± 0.09 and 0.82 ± 0.08, respectively. This average value is similar to the average S^2 values reported for other proteins (*37*, *55*, *66*, *82*, *83*). In general for vMIP-II, regions of secondary structure have higher order parameters, with average values of 0.90 ± 0.04, 0.88 ± 0.04, 0.83 ± 0.05, and 0.85 ± 0.02 for β-strands β1, β2, and β3 and the α-helix, respectively, according to the values shown in Figure 2B. The amides of residues in the intervening regions (excluding the N-terminus) have an average order parameter of 0.79 ± 0.12. The N-terminus has low apparent τ_c (Figure 2A), low S^2 values (Figure 2B), and low S_s^2 values (Figure 2C), which reveals that this section of the protein is highly mobile, with the first seven N−H vectors in vMIP-II showing near-complete disorder. This conclusion is corroborated by the near random coil chemical shifts and the rapid amide proton exchange rate in this region (Figure 1). Together, these data suggest that the N-terminus is extended freely into solution where it is unrestricted by interactions with the body of the protein. The region of the ordered turn from residues 25−28 experiences conformational exchange dynamics but also displays rather slow amide exchange rates (Figure 1). These observations suggest that these residues undergo motion on the millisecond time scale, perhaps with some degree of correlation.

vMIP-II Structure and Dynamics in Light of Function. vMIP-II is a monomer, even under concentrated conditions (0.8 mM protein), as indicated by a rotational correlation time of 4.7 ± 0.3 ns. While pH and solution conditions have been shown to affect dimer affinity in chemokines (*13*, *23*, *69*, *79*), almost all wild-type chemokines are dimers or multimers at NMR concentrations (*11*−*20*). As evidence has been presented that some chemokines are active as monomers (*21*−*24*), our results may be interpreted as confirming the monomeric species as the active form of vMIP-II. On the other hand, it is possible that this lack of preference for a particular dimer may allow vMIP-II at the cell surface to adopt either dimer type, which may account for its unique ability to cross-bind chemokine receptors. However, the amino acid sequence of the N-terminal region of vMIP-II is quite different than other CC chemokines, possessing charged amino acids near the conserved cysteines, where CC chemokines usually have hydrophobic or uncharged residues. This region is important in forming the CC chemokine dimer interface, and may be responsible for the lack of dimerization of vMIP-II.

The CXC chemokine IL-8 has previously been analyzed for its backbone dynamics (*37*), and although this protein is a dimer in solution, it exhibits marked similarity to the dynamics of vMIP-II, particularly at the N-terminus. Both vMIP-II and IL-8 have highly disordered N-termini that are characterized by very low order parameters, low ^{15}N{−H} *NOE* values, and long ^{15}N T_2 values. In addition, both proteins exhibit relatively high order parameters in the regions of secondary structure.

For some proteins, ligand binding results in an increase in order parameters, indicating a "stiffening" of the protein (*84*, *85*). Although vMIP-II has broad receptor binding ability and may use atypical regions in its receptor interaction, two

regions of chemokines have been postulated to be involved in receptor binding and activation: the N-terminus of the protein, comprising approximately the first 8−10 residues of most chemokines, and the "N-loop", a region spanning residues 16−24 (in our numbering system) (*32*, *34*, *36*, *86*, *87*). Some mutational work also implicates the first β-strand in receptor specificity (*88*, *89*). Our dynamics study of vMIP-II shows that most of the N-terminal amino acids through Lys13 are quite disordered. However, residues 25−28 are likely experiencing conformational exchange dynamics on a microsecond to millisecond time scale and this motion may have the effect of positioning or exposing the N-loop for receptor binding. Overall, the N-terminal region of vMIP-II shows the highest degree of disorder, and binding of vMIP-II to a receptor may decrease this disorder. In a study of the PLCγ1C SH2 domain Farrow et al. (*55*) showed that many residues in the unliganded SH2 domain required either the two-time-scale model or R_{ex}, while the binding of a phosphotyrosyl peptide greatly simplified the dynamics of the domain, largely removing the need for S_s^2 and reducing the number of residues requiring R_{ex}.

Conclusions. We report the backbone dynamics and a structural analysis of the anti-HIV chemokine vMIP-II. The rotational correlation time of vMIP-II is 4.7 ± 0.3 ns, indicating that this chemokine is monomeric even at the high concentrations required for NMR, which is unusual for chemokines and may bear on this protein's ability to cross-bind chemokine receptors. This protein appears to have a typical chemokine fold, consisting of an unstructured N-terminus and three antiparallel β-strands, followed by a C-terminal α-helix that lies across the strands with an orientation near perpendicular. The rotational diffusion anisotropy of vMIP-II is estimated to be about 1.5. The NMR data suggest that the N-terminus is extended into solution, possesses no secondary structure, and experiences a high degree of mobility. In addition, the ordered turn before strand β1 undergoes conformational exchange dynamics, perhaps in a concerted manner. Portions of the N-terminus of vMIP-II are expected to interact with chemokine receptors and may form a more ordered structure upon receptor binding.

ACKNOWLEDGMENT

We gratefully acknowledge Dan Garrett and Frank Delaglio for providing software and Carol Post and Jo Davisson for helpful discussions.

SUPPORTING INFORMATION AVAILABLE

Table S1, listing NH, N, Cα, Cβ, Hα, Hβ, and CO chemical shifts for vMIP-II residues (2 pages). Ordering information is available on any current masthead page.

REFERENCES

1. Oppenheim, J., J., Zachariae, C. O. C., Mukaida, N., and Matsushima, K. (1991) *Annu. Rev. Immunol. 9*, 617−648.
2. Schall, T. J. (1991) *Cytokine 3*, 165−183.
3. Cocchi, F., Devico, A. L., Garzinodemo, A., Lusso, P., and Gallo, R. C. (1995) *Science 270*, 1811−1815.
4. Alkhatib, G., Combadiere, C., Broder, C. C., Feng, Y., Kennedy, P. E., Murphy, P. M., and Berger, E. A. (1996) *Science 272*, 1955−1958.
5. Deng, H., et al. (1996) *Nature 381*, 661−666.
6. Drajic, T., et al. (1996) *Nature 381*, 667−673.
7. Bleul, C. C., Farzan, M., Choe, H., Parolin, C., Clark-Lewis, I., Sodroski, J., and Springer, T. A. (1996) *Nature 382*, 829−833.
8. Oberlin, E., Amara, A., Bachelerie, F., Bessia, C., Virelizier, J.-L., Arenzana-Seisdedos, Schwartz, O., Heard, J.-M., Clark-Lewis, I., Legler, D. F., Loetscher, M., Baggiolini, M., and Moser, B. (1996) *Nature 382*, 833−835.
9. Baggiolini, M. (1998) *Nature 329*, 565−568.
10. Hadley, T. J., and Peiper, S. C. (1997) *Blood 89*, 3077−3091.
11. Lodi, P. J., Garrett, D. S., Kuszewski, J., Tsang, M. L.-S., Weatherbee, J. A., Leonard, W. J., Gronenborn, A. M., and Clore, G. M. (1994) *Science 263*, 1762−1767.
12. Clore, G. M., Appella, E., Yamada, M., Matsushima, K., and Gronenborn, A. M. (1990) *Biochemistry 29*, 1689−1696.
13. Skelton, N. J., Aspiras, F., Ogez, J., and Schall, T. J. (1995) *Biochemistry 34*, 5329−5342.
14. Kim, K.-S., Clark-Lewis, I., and Sykes, B. D. (1994) *J. Biol. Chem. 269*, 32909−32915.
15. Meunier, A., Bernassau, J.-M., Guillemot, J.-C., Ferrara, P., and Darbon, H. (1997) *Biochemistry 36*, 4412−4422.
16. Chung, C., Cooke, R. M., Proudfoot, A. E. I., and Wells, T. N. C. (1995) *Biochemistry 34*, 3907−9314.
17. Handel, T. M., and Domaille, P. J. (1996) *Biochemistry 35*, 6569−6584.
18. Fairbrother, W. J., Reilly, D., Colby, T. J., Hesselgesser, J., and Horuk, R. (1994) *J. Mol. Biol. 242*, 252−270.
19. Lubkowski, J., Bujacz, G., Boque, L., Domaille, P. J., Handel, T. M., and Wlodawer, A. (1997) *Nat. Struct. Biol. 4*, 64−69.
20. Zhang, X., Chen, L., Bancroft, D. P., Lai, C. K., and Maione, T. E. (1994) *Biochemistry 33*, 8361−8366.
21. Rajarathnam, K., Kay, C. M., Dewald, B., Wolf, M., Baggiolini, M., Clark-Lewis, I., and Sykes, B. D. (1997) *J. Biol. Chem. 272*, 1725−1729.
22. Rajarathnam, K., Sykes, B. D., Kay, C. M., Dewald, B., Geiser, T., Baggiolini, M., and Clark-Lewis, I. (1994) *Science 264*, 90−92.
23. Lowman, H. B., Fairbrother, W. J., Slagle, P. H., Kabakoff, R., Liu, J., Shire, S., and Hebert, C. A. (1997) *Protein Sci. 6*, 598−608.
24. Avalos, B. R., Bartynski, K. J., Elder, P. J., Kotur, M. S., Burton, W. G., and Wilkie, N. M. (1994) *Blood 84*, 1790−1801.
25. Hoogewerf, A. J., Kuschert, G. S. V., Proudfoot, A. E. I., Borlat, F., Clark-Lewis, I., Power, C. A., and Wells, T. N. C. (1997) *Biochemistry 36*, 13570−13578.
26. Wagner, L., Yang, O. O., Garcia-Zepeda, E. A., Ge, Y., Kalams, S. A., Walker, B. D., Pasternack, M. S., and Luster, A. D. (1998) *Nature 391*, 908−911.
27. Zhang, Y., and Rollins, B. J. (1995) *Mol. Cell. Biol. 15*, 4851−4855.
28. Leong, S. R., Lowman, H. B., Liu, J., Shire, S., Deforge, L. E., Gillece-Castro, B. L., McDowell, R., and Hébert, C. A. (1997) *Protein Sci. 6*, 609−617.
29. Moore, P. S., Boshoff, C., Weiss, R. A., and Chang, Y. (1996) *Science 274*, 1739−1744.
30. Boshoff, C. E. Y., Collins, P. D., Takeuchi, Y., Reeves, J. D., Schweickart, V. L., Siani, M. A., Sasaki, T., Williams, T. J., Gray, P. W., Moore, P. S., Chang, Y., and Weiss, R. A. (1997) *Science 278*, 290−294.
31. Kledal, T. N., Rosenkilde, M. M., Coulin, F., Simmons, G., Johnsen, A. H., Alouani, S., Power, C. A., Luttichau, H. R., Gerstoft, J., Clapham, P. R., Clark-Lewis, I., Wells, T. N. C., and Schwartz, T. W. (1997) *Science 277*, 1656−1659.
32. Clark-Lewis, I., Kim, K.-S., Rajarathnam, K., Gong, J.-H., Dewald, B., Moser, B., Baggiolini, M., and Sykes, B. D. (1995) *J. Leukoc. Biol. 57*, 703−711.
33. Strieter, R. M., Polverini, P. J., Kunkel, S. L., Arenberg, D. A., Burdick, M. D., Kasper, J., Dzuiba, J., Van Damme, J., Walz, A., Marriott, D., Chan, S.-Y., Roczniak, S., and Shanafelt, A. B. (1995) *J. Biol. Chem. 270*, 27348−27357.
34. Gong, J.-H., Uguccioni, M., Dewald, B., Baggiolini, M., and Clark-Lewis, I. (1996) *J. Biol. Chem. 271*, 10521−10527.
35. Weber, M., Uguccioni, M., Baggiolini, M., Clark-Lewis, I., and Dahinden, C. A. (1996) *J. Exp. Med. 183*, 681−685.

36. Pakianathan, D. R., Kuta, E. G., Artis, D. R., Skelton, N. J., and Hebert, C. A. (1997) *Biochemistry 36*, 9642−9648.
37. Grasberger, B. L., Gronenborn, A. M., and Clore, G. M. (1993) *J. Mol. Biol. 230*, 364−372.
38. van Kimmenade, B., Bond, M. W., Schumacher, J. H., Laquoi, C., and Kastelein, R. A. (1988) *Eur. J. Biochem. 173*, 109−114.
39. Wishart, D. S., Bigam, C. G., Yao, J., Abildgaard, F., Dyson, H. J., Oldfield, E., Markley, J. L., and Sykes, B. D. (1995) *J. Biomol. NMR 6*, 135−140.
40. Grzesiek, S., and Bax, A. (1993) *J. Am. Chem. Soc. 115*, 12593−12594.
41. Zhu, G., and Bax, A. (1990) *J. Magn. Reson. 90*, 405−410.
42. Grzesiek, S., and Bax, A. (1992) *J. Am. Chem. Soc. 114*, 6291−6293.
43. Grzesiek, S., and Bax, A. (1992) *J. Magn. Reson. 99*, 201−207.
44. Grzesiek, S., and Bax, A. (1993) *J. Biomol. NMR 3*, 185−204.
45. Kay, L. E., Ikura, M., Tschudin, R., and Bax, A. (1990) *J. Magn. Reson. 89*, 496−514.
46. Ikura, M., Kay, L. E., Tschudin, R., and Bax, A. (1990) *J. Magn. Reson. 86*, 204−209.
47. Zuiderweg, E. R. P., and Fesik, S. W. (1989) *Biochemistry 28*, 2387−2391.
48. Bax, A., and Grzesiek, S. (1993) *Acc. Chem. Res. 26*, 131−138.
49. Cavanagh, J. F., and Rance, M. (1992) *J. Magn. Reson. 96*, 670−678.
50. Vuister, G. W., and Bax, A. (1993) *J. Am. Chem. Soc. 115*, 7772−7777.
51. Kuboniwa, H., Grzesiek, S., Delaglio, F., and Bax, A. (1994) *J. Biomol. NMR 4*, 871−878.
52. Wang, A. C., and Bax, A. (1996) *J. Am. Chem. Soc. 118*, 2483−2494.
53. Kay, L. E., Nicholson, L. K., Delaglio, F., Bax, A., and Torchia, D. A. (1992) *J. Magn. Reson. 97*, 359−375.
54. Tjandra, N., Wingfield, P., Stahl, S., and Bax, A. (1996) *J. Biomol. NMR 8*, 273−284.
55. Farrow, N. A., Muhandiram, R., Singer, A. U., Pascal, S. M., Kay, C. M., Gish, G., Shoelson, S. E., Pawson, T., Forman-Kay, J. D., and Kay, L. E. (1994) *Biochemistry 33*, 5984−6003.
56. Gagné, S. M., Tsuda, S., Spyrcopoulos, L., Kay, L. E., and Sykes, B. D. (1998) *J. Mol. Biol. 278*, 667−686.
57. Wang, A. C., and Bax, A. (1993) *J. Biomol. NMR 3*, 715−720.
58. Kay, L. E., Torchia, D. A., and Bax, A. (1989) *Biochemistry 28*, 8972−8979.
59. Tjandra, N., Kuboniwa, H., Ren, H., and Bax, A. (1995) *Eur. J. Biochem. 230*, 1014−1024.
60. Tjandra, N., Feller, S. E., Pastor, R. W., and Bax, A. (1995) *J. Am. Chem. Soc. 117*, 12562−12566.
61. Lipari, G., and Szabo, A. (1982) *J. Am. Chem. Soc. 104*, 4546−4559.
62. Schurr, J. M., Babcock, H. P., and Fujimoto, B. S. (1994) *J. Magn. Reson., Ser. B 105*, 211−224.
63. Luginbühl, P., Pervushin, K. V., Iwai, H., and Wüthrich, K. (1997) *Biochemistry 36*, 7305−7312.
64. Tjandra, N., Garrett, D. S., Gronenborn, A. M., Bax, A., and Clore, G. M. (1997) *Nat. Struct. Biol. 4*, 443−449.
65. Lipari, G., and Szabo, A. (1982) *J. Am. Chem. Soc. 104*, 4559−4570.
66. Clore, G. M., Driscoll, P. C., Wingfield, P. T., and Gronenborn, A. M. (1990) *Biochemistry 29*, 7387−7401.
67. Clore, G. M., Szabo, A., Bax, A., Kay, L. E., Driscoll, P. C., and Gronenborn, A. M. (1990) *J. Am. Chem. Soc. 112*, 4989−4991.
68. Powers, R., Clore, G. M., Stahl, S. J., Wingfield, P. T., and Gronenborn, A. (1992) *Biochemistry 31*, 9150−9157.
69. Laurence, J. S., LiWang, A. C., and LiWang, P. J. (1998) *Biochemistry 37*, 9346−9354.
70. Clore, G. M., and Gronenborn, A. M. (1994) *Prog. Biophys. Mol. Biol. 62*, 153−184.
71. Wishart, D. S., and Sykes, B. D. (1994) *Methods Enzymol. 239*, 363−393.
72. Asakura, T., Taoka, K., Demura, M., and Williamson, M. P. (1995) *J. Biolmol. NMR 6*, 227−236.
73. Williamson, M. P. (1990) *Biopolymers 29*, 1423−1431.
74. Spera, S., and Bax, A. (1991) *J. Am. Chem. Soc. 113*, 5490−5492.
75. Pardi, A., Billeter, M., and Wüthrich, K. (1984) *J. Mol. Biol. 180*, 741−751.
76. Andrec, M., Hill, R. B., and Prestegard, J. H. (1995) *Protein Sci. 4*, 983−993.
77. Crump, M. P., et al. (1997) *EMBO J. 16*, 6996−7007.
78. Minor, D. L., and Kim, P. S. (1994) *Nature 367*, 660−663.
79. Mayo, K. H., and Chen, M.-J. (1989) *Biochemistry 28*, 9469−9478.
80. Kim, K.-S., Rajarathnam, K., Clark-Lewis, I., and Sykes, B. D. (1996) *FEBS Lett. 395*, 277−282.
81. Dealwis, C., Fernandez, E. J., Thompson, D. A., Simon, R. J., Siani, M. A. and Lolis, E. (1998) *Proc. Natl. Acad. Sci. U.S.A. 95*, 6941−6946.
82. Campbell, J. J., Hedrick, J., Zlotnik, A., Siani, M. A., Thompson, D. A. and Butcher, E. C. (1998) *Science 279*, 381−383.
83. Stone, M. J., Fairbrother, W. J., Palmer, A. G., Reizer, J., Saier, M. H., and Wright, P. E. (1992) *Biochemistry 31*, 4394−4406.
84. Akke, M. S., N. J., Kordel, J., Palmer, A. G., and Chazin, W. J. (1993) *Biochemistry 32*, 9832−9844.
85. Nicholson, L. K., Kay, L. E., Baldisseri, D. M., Arango, J., Young, P. E., Bax, A., and Torchia, D. A. (1992) *Biochemistry 31*, 5253−5263.
86. Clark-Lewis, I., Schumacher, C., Baggiolini, M., and Moser, B. (1991) *J. Biol. Chem. 266*, 23128−23134.
87. Schraufstatter, I. U., Ma, M., Oades, Z. G., Barritt, D. S., and Cochrane, C. G. (1995) *J. Biol. Chem. 270*, 10428−10431.
88. Wells, T. N. C., Power, C. A., Lusti-Narasimhan, M., Hoogewerf, A. J., Cooke, R. M., Chung, C., Peitsch, M. C., and Proudfoot, A. E. I. (1996) *J. Leukoc. Biol. 59*, 53−60.
89. Lusti-Narasimhan, M., Power, C. A., Allet, B., Alouani, S., Bacon, K. B., Mermod, J.-J., Proudfoot, A. E. I., Wells, T. N. C. (1995) *J. Biol. Chem. 270*, 2716−2721.

BI9812726